ARTICLES
PUBLISHED ONLINE: 5 JUNE 2017 | DOI: 10.1038/NPHYS4150

nature physics

Microwave spectroscopy of spinful Andreev bound states in ballistic semiconductor Josephson junctions

David J. van Woerkom[1,2], Alex Proutski[1,2], Bernard van Heck[3], Daniël Bouman[1,2], Jukka I. Väyrynen[3], Leonid I. Glazman[3], Peter Krogstrup[4], Jesper Nygård[4], Leo P. Kouwenhoven[1,2] and Attila Geresdi[1,2]*

The superconducting proximity effect in semiconductor nanowires has recently enabled the study of new superconducting architectures, such as gate-tunable superconducting qubits and multiterminal Josephson junctions. As opposed to their metallic counterparts, the electron density in semiconductor nanosystems is tunable by external electrostatic gates, providing a highly scalable and *in situ* variation of the device properties. In addition, semiconductors with large *g*-factor and spin–orbit coupling have been shown to give rise to exotic phenomena in superconductivity, such as φ_0 Josephson junctions and the emergence of Majorana bound states. Here, we report microwave spectroscopy measurements that directly reveal the presence of Andreev bound states (ABS) in ballistic semiconductor channels. We show that the measured ABS spectra are the result of transport channels with gate-tunable, high transmission probabilities up to 0.9, which is required for gate-tunable Andreev qubits and beneficial for braiding schemes of Majorana states. For the first time, we detect excitations of a spin-split pair of ABS and observe symmetry-broken ABS, a direct consequence of the spin–orbit coupling in the semiconductor.

The linear conductance $G=(2e^2/h)\sum T_i$ of a nanostructure between two bulk leads[1] depends on the individual channel transmission probabilities, T_i. Embedding the same structure between two superconducting banks with a superconducting gap of Δ gives rise to Andreev bound states (ABS)[2]. If the junction length is much smaller than the superconducting coherence length, ξ, that is, in the short-junction limit, then the ABS levels depend on the phase difference ϕ between the leads according to[3]:

$$E_{\mathrm{ABS},i}(\phi)=\pm\Delta\sqrt{1-T_i\sin^2\frac{\phi}{2}} \quad (1)$$

These subgap states with $|E_{\mathrm{ABS}}|\leq\Delta$ are localized in the vicinity of the nanostructure and extend into the banks over a length scale determined by ξ. Note that equation (1) is valid only in the absence of magnetic field, when each energy level is doubly degenerate.

Direct microwave spectroscopy has recently demonstrated the occupation of the ABS by exciting a Cooper pair in atomic junctions[4]. Unlike quasiparticle tunnelling spectroscopy, which has also been used to detect ABS[5,6], resonant excitation by microwaves is a charge parity-conserving process[7]. This property enables coherent control of ABS which is required for novel qubit architectures[8] and makes microwave spectroscopy a promising tool to detect Majorana bound states[9] in proximitized semiconductor systems[10–12].

We investigate ABS excitations in Josephson junctions that consist of indium arsenide (InAs) nanowires covered by epitaxial aluminium (Al) shells[13]. The junction, where the superconducting shell is removed, is 100 nm (device 1, see the red box in Fig. 1a) and 40 nm long (device 2), respectively. The nanowire is then embedded in a hybrid superconducting quantum interference device (SQUID) whose second arm is a conventional Al/AlO$_x$/Al tunnel junction (in yellow box), enabling the control of the phase drop ϕ by means of the applied magnetic flux Φ through the SQUID loop. In the limit of a negligible loop inductance and an asymmetric SQUID, where the Josephson coupling of the nanowire is much smaller than that of the tunnel junction, the applied phase φ mostly drops over the nanowire link: $\phi\approx\varphi=2\pi\Phi/\Phi_0$, where $\Phi_0=h/2e$ is the superconducting flux quantum. We measure the microwave response[4,7] of the nanowire junction utilizing the circuit depicted in Fig. 1a, where a second Al/AlO$_x$/Al tunnel junction (in green box) is capacitively coupled to the hybrid SQUID and acts as a spectrometer. Further details on the fabrication process are given in the Supplementary Methods.

In this circuit, inelastic Cooper-pair tunnelling (ICPT, Fig. 1d) of the spectrometer junction is enabled by the dissipative environment and results in a d.c. current, I_{spec} (ref. 14):

$$I_{\mathrm{spec}}=\frac{I_{\mathrm{c,spec}}^2\mathrm{Re}[Z(\omega)]}{2V_{\mathrm{spec}}} \quad (2)$$

Here $I_{\mathrm{c,spec}}$ is the critical current of the spectrometer junction, V_{spec} is the applied voltage bias, and $Z(\omega)$ is the circuit impedance at a frequency $\omega=2eV_{\mathrm{spec}}/\hbar$. Since $Z(\omega)$ peaks at the resonant frequencies of the hybrid SQUID[4,14], so does the d.c. current I_{spec}, allowing us to measure the ABS excitation energies of the nanowire junction (Fig. 1b), as well as the plasma frequency of the SQUID (Fig. 1c).

First we characterize the contribution of the plasma mode with the nanowire junction gated to full depletion, that is, $G=0$. We show the $I(V)$ curve of the spectrometer junction of device 1 in Fig. 1f, where we find a single peak centred at $\hbar\omega_p/2=eV_{\mathrm{spec}}=46\,\mu$eV and a quality factor $Q\approx1$. In the limit of $E_C\ll E_J$, $\hbar\omega_p=\sqrt{2E_CE_J}$, where E_C is the charging energy of the circuit and E_J is the Josephson coupling of the tunnel junction (Fig. 1e). Estimating $E_J=165\,\mu$eV from the normal state resistance[15], this measurement allows us to determine

[1]QuTech, Delft University of Technology, 2600 GA Delft, The Netherlands. [2]Kavli Institute of Nanoscience, Delft University of Technology, 2600 GA Delft, The Netherlands. [3]Department of Physics, Yale University, New Haven, Connecticut 06520, USA. [4]Center for Quantum Devices and Station Q Copenhagen, Niels Bohr Institute, University of Copenhagen, Universitetsparken 5, 2100 Copenhagen, Denmark. *e-mail: A.Geresdi@tudelft.nl

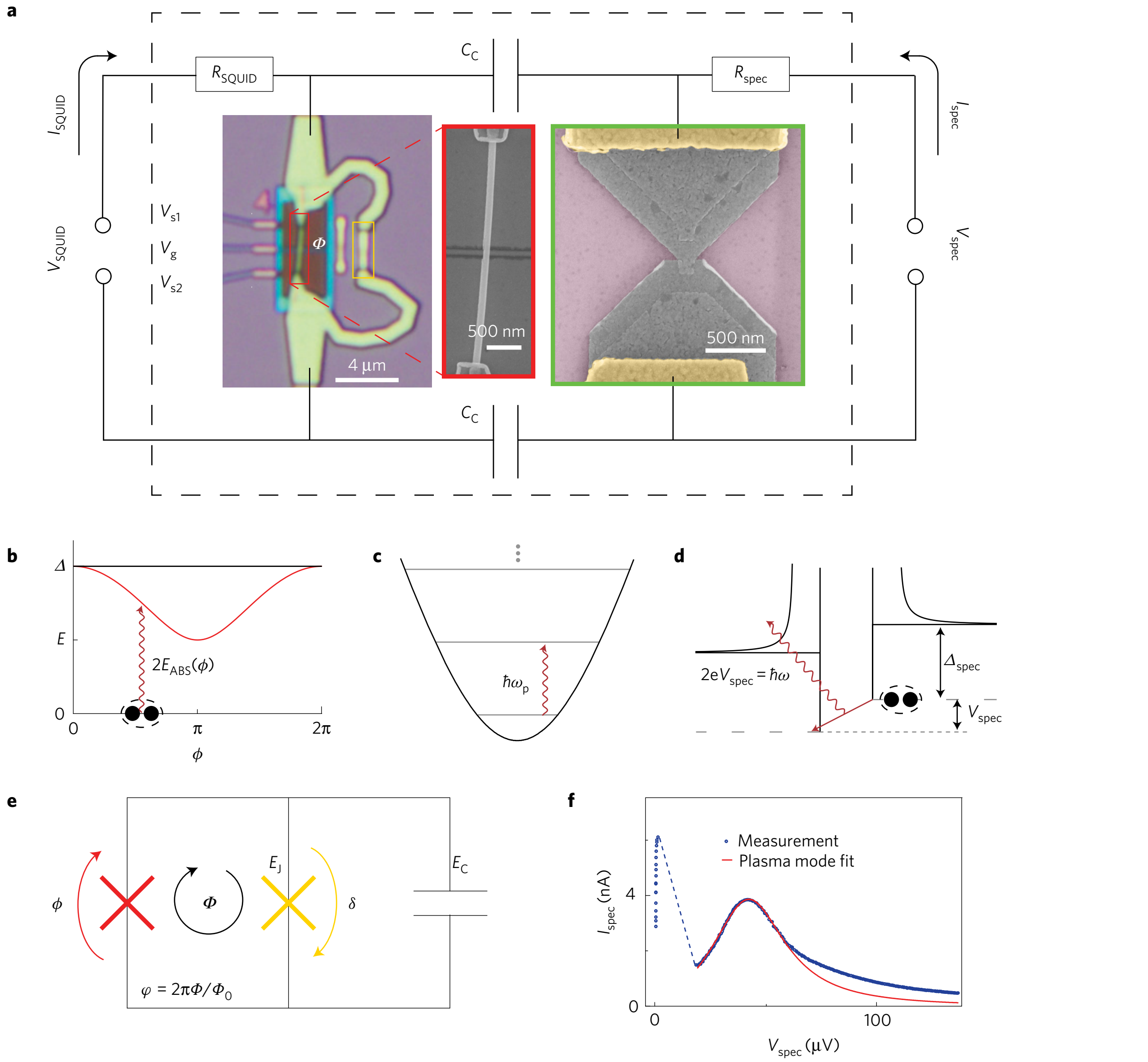

Figure 1 | Device schematics and working principle. **a**, Equivalent circuit diagram: bright-field optical image of the hybrid SQUID with one InAs semiconductor nanowire weak link (scanning electron micrograph, in the red box) and an Al/AlO_x/Al tunnel junction (enclosed by the yellow box). The SQUID is capacitively coupled to the spectrometer Al/AlO_x/Al Josephson junction (scanning electron micrograph, in the green box) via C_c. The transmission of the semiconductor channel is tuned by the gate voltage, V_g. Additional gates near the electrodes are kept at a constant voltage $V_{s1,2}$. Circuit elements within the dashed box are located on-chip, thermally anchored to 12 mK. **b**–**d**, Excitations of the hybrid SQUID: the Andreev bound state at $\hbar\omega = 2E_{ABS}$ (**b**) and the plasma oscillations at $\hbar\omega = \hbar\omega_p$ (**c**) are excited by a photon energy $\hbar\omega = 2eV_{spec}$ set by the d.c. voltage bias of the spectrometer (**d**) with a superconducting gap Δ_{spec}. **e**, Schematic circuit diagram of the hybrid SQUID. The total phase $\varphi = \phi + \delta$ is determined by the applied flux Φ. **f**, The measured $I(V)$ trace of the spectrometer junction with the nanowire in full depletion—that is, in the absence of ABS excitations. The red solid line shows the fit to the circuit model of a single resonance centred at $\hbar\omega_p$, see text. Images and data were all taken on device 1.

$E_C = 25.4\,\mu$eV (see the Supplementary Methods). The choice of a low quality factor in combination with a characteristic impedance $Z_0 = 551\,\Omega \ll R_q = h/4e^2$ ensures the suppression of higher-order transitions and parasitic resonances.

Next, we investigate the spectrometer response as a function of the gate voltage V_g applied to the nanowire. Note that the spectrometer response to the ABS transitions is superimposed on the plasma resonance peak. To achieve a better visibility of the ABS lines, we display $-\mathrm{d}^2I_{spec}/\mathrm{d}V_{spec}^2(V_{spec})$ rather than $I_{spec}(V_{spec})$ (see Supplementary Methods for comparison). In the presence of ABS, the spectrum exhibits peaks at frequencies where $\hbar\omega = 2E_{ABS,i}$ (ref. 7). In Fig. 2a, we monitor the appearance of these peaks for an applied phase $\varphi = \pi$, where the ABS energy of equation (1) is $E_{ABS,i}(\pi) = \Delta\sqrt{1-T_i}$. Notably, for V_g values close to full depletion (see red bar in Fig. 2a), we see a gradual decrease of $E_{ABS}(\pi)$ with increasing V_g (black circles in Fig. 2e). In this regime, we find a good correspondence with equation (1), assuming single-channel transport, $G = (2e^2/h)T$ (red solid line in Fig. 2e, see the Supplementary Methods on the details of the measurement of G). However, the observed $\Delta = 122\,\mu$eV is smaller than the $\Delta_{Al} \approx 200\,\mu$eV of the thin-film Al contacts, in agreement with the presence of induced superconductivity in the nanowire[16]. Increasing V_g further, we observe a sequential appearance of peaks, which we attribute to the opening of multiple transport channels in the weak link and the consequent formation of multiple ABS[3] as the Fermi level E_F increases. We also find a strong variation of E_{ABS} with V_g similarly to earlier experiments[17–19]. We attribute this observation to mesoscopic fluctuations in the presence of weak disorder[3], such that the mean free path of the charge carriers is comparable to the channel length.

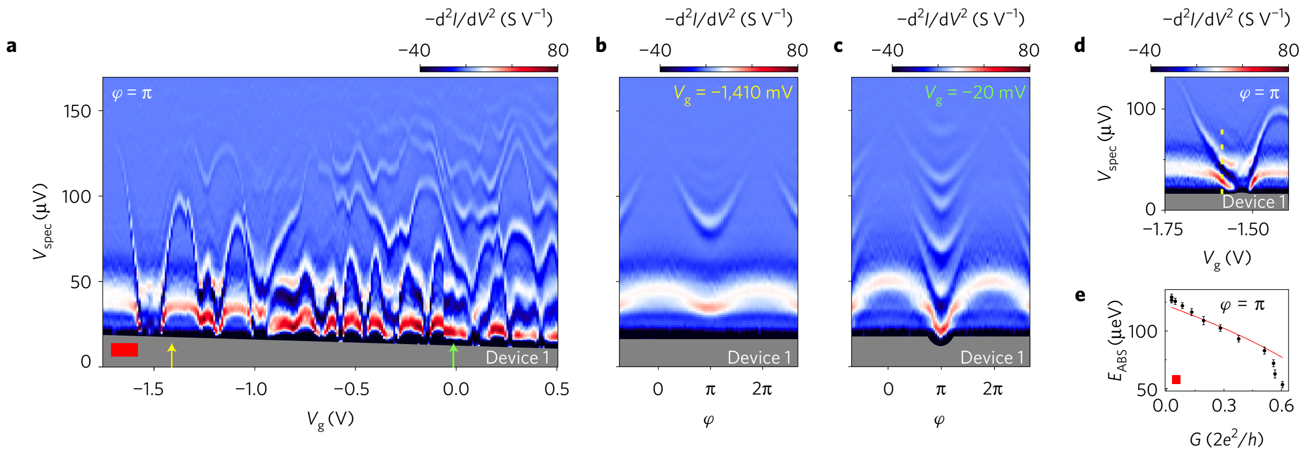

Figure 2 | Gate dependence of Andreev bound states. a, $-d^2I/dV^2$ of the spectrometer junction as a function of V_g at $\varphi = \pi$, where $E_{ABS,i} = \Delta\sqrt{1-T_i}$ in the short-junction limit. **b**,**c**, $-d^2I/dV^2$ of the spectrometer junction as a function of $\varphi = 2\pi\Phi/\Phi_0$ for one channel (**b**) and several channels (**c**). The qualitative agreement of the line shapes with equation (1) confirms the short-junction behaviour. Arrows in **a** indicate V_g for these measurements. Weakly visible vertically shifted replicas of the ABS lines indicate higher-order transitions, see text. **d**, Strong hybridization between the ABS excitation and the plasma mode with a level repulsion of $\varepsilon = 22\,\mu$eV at the yellow dashed line. **e**, $E_{ABS}(\varphi = \pi)$ as a function of the d.c. linear conductance G of the nanowire weak link in the gate span denoted by the red bar in **a**. The error bars correspond to the linewidth of the measured signal. The solid red line shows the prediction of the single-channel model with $\Delta = 122\,\mu\text{eV} \pm 3\,\mu\text{eV}$, see text. All data was taken on device 1. Grey regions denote lack of data due to bias instability of the circuit.

Now we turn to the flux dependence of the observed spectrum, shown in Fig. 2b,c for two distinct gate configurations. We find a qualitative agreement with equation (1) with one transport channel in Fig. 2b and several channels in Fig. 2c, confirming that our device is in the short-junction limit. In addition, we observe the plasma mode at $eV_{spec} < 50\,\mu$eV. We also find that the plasma mode $\hbar\omega_p$ oscillates with φ when the nanowire is gated to host open transport channels. This is expected due to the Josephson coupling of the nanowire becoming comparable to E_J, which also causes a finite phase drop, δ, over the tunnel junction (see Supplementary Methods). We also note the presence of additional, weakly visible lines in the spectrum which could be attributed to higher-order processes[4]. However, we did not identify the nature of these excitations, and we focus on the main transitions throughout the current work.

In addition, we observe the occurrence of avoided crossings between the Andreev and plasma modes, as shown in Fig. 2d at $\varphi = \pi$. These avoided crossings require $\hbar\omega_p \approx 2\Delta\sqrt{1-T}$, which translates to a high transmission probability $T \approx 0.8$–0.9, and demonstrates the hybridization between the ABS excitation and the plasma mode. The coupling between these two degrees of freedom has previously been derived[7,20] (see Supplementary Methods), leading to a perturbative estimate for the energy splitting $\varepsilon \approx \Delta T(E_C/2E_J)^{1/4} \approx 40$–$70\,\mu$eV, similar to the observed value of $22\,\mu$eV. The discrepancy is fully resolved in the numerical analysis of the circuit model developed below.

We provide a unified description of the energy spectrum of the circuit as a whole, and consider the following Hamiltonian for the hybrid SQUID (Fig. 1e)[20]:

$$\hat{H} = E_C\hat{N}^2 + E_J(1 - \cos\hat{\delta}) + \hat{H}_{ABS}(\varphi - \hat{\delta}) \qquad (3)$$

Here $\hat{\delta}$ is the operator of the phase difference across the tunnel junction, conjugate to the charge operator $\hat{N}$, $[\hat{\delta}, \hat{N}] = i$. The first two terms in equation (3) represent the charging energy of the circuit and the Josephson energy of the tunnel junction (Fig. 1e). The last term describes the quantum dynamics of a single-channel short weak link[21,22], which depends on Δ and T. For the analytic form of $\hat{H}_{ABS}$, see the Supplementary Methods. To fully account for the coupling between the ABS excitation and the quantum dynamics of the phase across the SQUID, we numerically solve the eigenvalue problem $\hat{H}\Psi = E\Psi$ and determine the transition frequencies $\hbar\omega = E - E_{GS}$, with E_{GS} being the ground state energy.

This procedure allows us to fit the experimental data, and we find a good quantitative agreement, as shown in Fig. 3a for a data set taken at $V_g = -1410$ mV with the fit parameters $\Delta = 122\,\mu$eV and $T = 0.57$. The previously identified circuit parameters E_J and E_C are kept fixed during the fit. We note that the observed ABS transition (orange solid line) deviates only slightly from equation (1) (black dashed line). The modulation of the plasma frequency (green solid line) is then defined by the model Hamiltonian with no additional fit parameters. We further confirm the nature of the plasma and ABS excitations by evaluating the probability density $|\Psi(\delta, \sigma)|^2$ of the eigenfunctions of equation (3) at $\varphi = \pi$ (Fig. 3b). In the ground state of $\hat{H}$ (GS) and in the state corresponding to the plasma excitation (green line in Fig. 3a), the probability density is much higher in the ground state of the weak link ($\sigma = g$, blue line) than in the excited state ($\sigma = e$, red line). In contrast, the next observed transition (orange line in Fig. 3a) gives rise to a higher contribution from $\sigma = e$, confirming our interpretation of the experimental data in terms of ABS excitations. Furthermore, the model can also describe measurement data with T close to 1, where it accurately accounts for the avoided crossings between the ABS and plasma spectral lines (see the Supplementary Methods for a dataset with $T = 0.9$).

In Fig. 3c we show the visibility of the ABS transition as a function of the applied phase φ, which is proportional to the absorption rate of the weak link, predicted to be $\propto T^2(1-T)\sin^4(\varphi/2) \times \Delta^2/E^2_{ABS}(\varphi)$ (ref. 7). We note that in the experimental data the maximum of the intensity is slightly shifted from its expected position at $\varphi = \pi$. This minor deviation may stem from the uncertainty of the flux calibration. Nevertheless, using $T = 0.57$, obtained from the fit in Fig. 3a, we find a good agreement with no adjustable parameters (black dashed line). A similarly good correspondence is also found with the full numerical model (orange line) based on equation (3).

We now discuss the evolution of the ABS as a function of an in-plane magnetic field B aligned parallel to the nanowire axis, which is perpendicular to the internal Rashba spin–orbit field (see the inset in Fig. 4b for measurement geometry). The applied field lifts the Kramers degeneracy of the energy spectrum, splitting each Andreev doublet into a pair $E^{\pm}_{ABS}(\phi)$. For small B, the splitting $E^{+}_{ABS}(\phi) - E^{-}_{ABS}(\phi)$ is linear in B, due to the Zeeman effect.

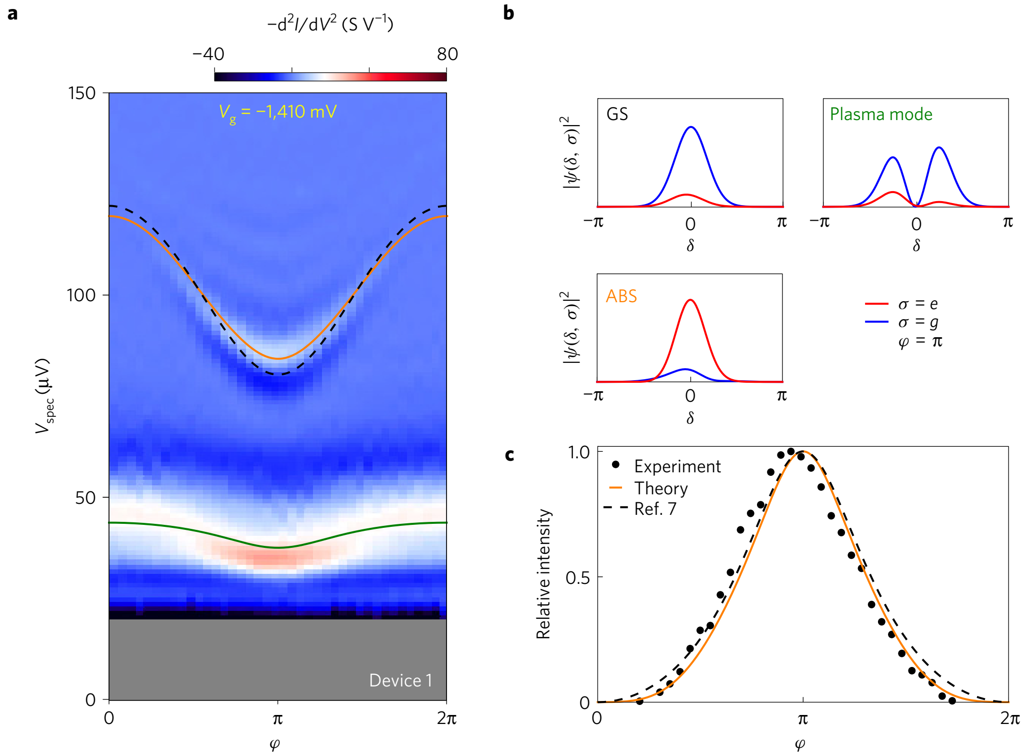

Figure 3 | Theoretical description of the transitions. a, Solid lines denote the transitions identified by the model described in the text, with Δ and T being free parameters. The experimental dataset is the same as the one shown in Fig. 2b. The dashed line shows equation (1) for the fitted $\Delta = 122\,\mu$eV and $T = 0.57$. **b**, The probability density $|\Psi(\delta,\sigma)|^2$ in the ground state of the hybrid SQUID (GS), and in the two excited states depicted in **a**, respectively. The weight in the ABS ground state ($\sigma = g$) and in the ABS excited state ($\sigma = e$) distinguishes between the plasma mode and the ABS. **c**, The measured relative intensity of the ABS transition (black circles) compared to the theoretical expectation based on equation (3) (orange solid line) and from ref. 7 (black dashed line) with no additional fitting parameters.

However, the spin-split single particle levels are not accessible by microwave spectroscopy, which can only induce transitions to a final state with two excited quasiparticles. Thus, we can only measure $E_{\rm tot}(\phi) = E^{+}_{\rm ABS}(\phi) + E^{-}_{\rm ABS}(\phi)$ and expect no split of the measured spectral lines. The experimental data (Fig. 4a) shows that $E_{\rm tot}$ decreases with B, while the lineshape remains qualitatively intact.

To explain the field dependence of $E_{\rm tot}$, we study the behaviour of ABS in a simple model consisting of a short Josephson junction in a one-dimensional quantum wire with proximity-induced superconductivity, Rashba spin–orbit and an applied Zeeman field parallel to the wire[10,11,23]. Within this model, we are able to find $E^{+}_{\rm ABS}$ and $E^{-}_{\rm ABS}$, and reproduce the observed quadratic decrease of the measured $E_{\rm tot}(\pi)$ (black circles in Fig. 4b). Initially, as B is increased, the proximity-induced gap $\Delta(B)$ is suppressed (black solid line), while the energy $E^{+}_{\rm ABS}(\pi)$ (blue solid line) increases due to the Zeeman split of the ABS. However, a crossing of the discrete ABS level with the continuum is avoided due to the presence of spin–orbit coupling, which prevents level crossings in the energy spectrum by breaking spin-rotation symmetry. The repulsion between the ABS level and the continuum causes a downward bending of $E^{+}_{\rm ABS}(\pi)$, in turn causing a decrease in $E_{\rm tot}(\pi)$ (black dashed line).

We perform the calculations in the limit where the Fermi level $E_{\rm F}$ in the wire is well above the Zeeman energy $E_{\rm Z} = (1/2)g\mu_{\rm B}B$ and the spin–orbit energy $E_{\rm SO} = m\alpha^2/2\hbar^2$ with m the effective mass and α the Rashba spin–orbit coupling constant. In this case and in the short-junction limit, the ratio $E_{\rm tot}(\pi)/\Delta$ is a function of just two dimensionless parameters: $E_{\rm Z}/\Delta$ and $\sqrt{E_{\rm SO}E_{\rm F}}/\Delta$. First we extract $\Delta = 152\,\mu$eV and $T = 0.56$ at $B = 0$ (leftmost panel in Fig. 4a). Then we perform a global fit on $E_{\rm tot}(\phi)$ at all B values and obtain a quantitative agreement with the theory for $g = 14.7 \pm 0.6$, which is in line with expected g-factor values in InAs nanowires[24–26] and $\sqrt{E_{\rm SO}E_{\rm F}}/\Delta = 0.32 \pm 0.02$. This model is consistent, assuming $E_{\rm F} > E_{\rm Z} \approx 100\,\mu$eV at 300 mT. Thus, we attain an upper bound $E_{\rm SO} \lesssim 24\,\mu$eV, equivalent to a Rashba parameter $\alpha \lesssim 0.12$ eVÅ in correspondence with earlier measurements on the same nanowires[26]. However, assuming the opposite limit, $E_{\rm F} \approx 0$, the theory is not in agreement with the experimental data (see the Supplementary Methods).

The theoretical energy spectrum shown in Fig. 4b predicts a ground state fermion-parity switch of the junction at a field $B_{\rm sw} \approx 400$ mT, at which the lowest ABS level $E^{-}_{\rm tot}(\pi) = 0$ (red line in Fig. 4b). This parity switch inhibits the resonant excitation of the Zeeman-split ABS levels[27], thus preventing microwave spectroscopy measurements for $B > B_{\rm sw}$. This prediction is in agreement with the vanishing visibility of the ABS line at $B \approx B_{\rm sw}$ in the experiment.

In addition to the interplay of spin–orbit and Zeeman couplings, the orbital effect of the magnetic field[28] is a second possible cause for the decrease of the ABS transition energy. Orbital depairing influences the proximity-induced pairing and results in a quadratic decrease of the induced superconducting gap: $\Delta(B) = \Delta(1 - B^2/B_*^2)$, where $B_* \sim \Phi_0/A$ and A is the cross-section of the nanowire. A simple model which includes both orbital and Zeeman effect, but no spin–orbit coupling, yields $B_* \approx 400$ mT when fitted to the experimental data (see Supplementary Methods for details). In this case, the fit is insensitive to the value of the g-factor. However, the model also predicts the occurrence, at $\varphi = \pi$, of a fermion-parity switch at a field $B_{\rm sw} < B_*$ whose value depends on the g-factor. Because agreement with the experimental data imposes the condition that $B_{\rm sw} > 300$ mT, in the Supplementary Methods we show that this scenario requires $g \lesssim 5$, which is lower than g-factor values measured earlier in InAs nanowire channels[24–26].

Furthermore, we can consider the qualitative effect of the inclusion of a weak spin–orbit coupling ($E_{\rm SO} \ll \Delta$) in this model containing only the orbital and Zeeman effects. We note that,

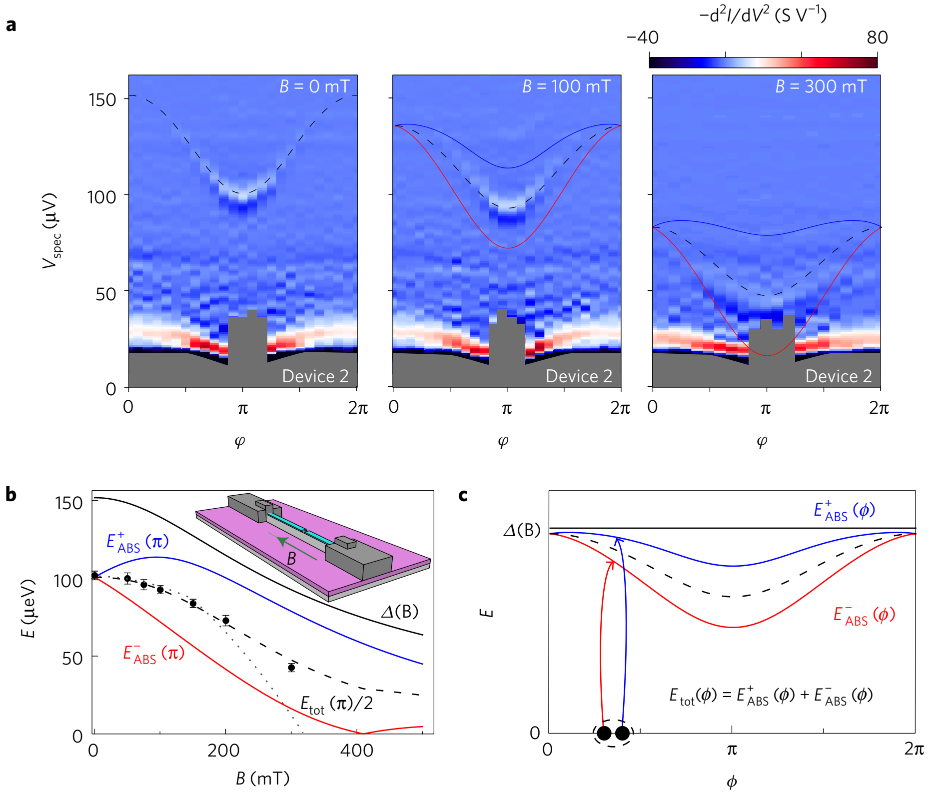

Figure 4 | Spectroscopy of spin-split Andreev bound states in a Rashba nanowire. a, Flux dependence of the Andreev bound states at $B=0$, 100 and 300 mT, respectively, applied parallel to the nanowire. The zero-field fit yields to $T=0.56$ and $\Delta=152\,\mu$eV. Dashed lines depict the fit of $E_{tot}(\phi)=E^+_{ABS}(\phi)+E^-_{ABS}(\phi)$ to the model described in the text. **b**, Black circles show the measured $E_{tot}(\pi)$ as a function of B. The error bars correspond to the linewidth of the measured signal. The dashed line depicts the fit to the theory with $g=14.7\pm0.6$ and $\sqrt{E_{SO}E_F}/\Delta=0.32\pm0.02$, see text. The Zeeman-split ABS levels $E^{\pm}_{ABS}(\pi)$ and the proximity-induced gap $\Delta(B)$ obtained from the model are shown as visual guides. The dotted line depicts the expected behaviour of $E_{tot}(B)$ in the presence of a strong orbital magnetic field with $B_*=400$ mT and weak spin-orbit coupling, see text. **c**, $E^{\pm}_{ABS}(\phi)$ computed at $B=100$ mT are shown as blue and red solid lines, together with the calculated transition energy $E_{tot}(\phi)$ (black dashed line). The experimental data was taken on device 2 at $V_g=140$ mV. Grey regions denote lack of data due to bias instability of the circuit.

without spin–orbit coupling, the upper Andreev level $E^+_{ABS}(B)$ crosses a continuum of states $\Delta(B)$ with opposite spin upon increasing the magnetic field (see Supplementary Fig. 11c). The crossing happens at a field of B_{cross} whose value depends on the g-factor: using the upper bound for g derived in the last paragraph, $g\approx5$, we can estimate $B_{cross}\approx150$ mT. At this magnetic field, a weak spin–orbit coupling results in an avoided crossing between the Andreev level $E^+_{ABS}(B)$ and the continuum. As a consequence, when $B>B_{cross}$, the energy $E^+_{ABS}(B)$ is bounded by the edge of the continuum and it is markedly lower than its value in the absence of spin–orbit coupling. In turn, this results in a decrease of the transition energy $E_{tot}(B)$ at $B>B_{cross}$, to the extent that such a model containing the joint effect of orbital depairing and weak spin–orbit coupling would depart from the experimental data in the range $150\,\text{mT}<B<300\,\text{mT}$ (see dotted line in Fig. 4b). Thus, although based on the geometry of the experiment we cannot rule out the presence of an orbital effect of the magnetic field, these considerations imply that it does not play a dominant role in the quadratic suppression of the transition energy in the present measurements.

We finally note that in all cases we neglect the effect of B on the Al thin film, justified by its in-plane critical magnetic field exceeding 2 T (ref. 29).

We present the ABS spectrum in the presence of several transport channels in Fig. 5. While at zero magnetic field (left panel) the data is symmetric around $\varphi=\pi$, in a finite magnetic field (right panel) the data exhibits an asymmetric flux dependence (see the yellow dashed line as a guide to the eye). This should be contrasted with Fig. 4a, where the data for a single-channel wire are presented at different values of the magnetic field: each of the traces is symmetric around $\varphi=\pi$. This behaviour agrees with theoretical calculations in the short-junction limit, which show that this asymmetry can arise in a Josephson junction with broken time-reversal and spin-rotation symmetries as well as more than one transport channel[30]. While the data is asymmetric with respect to $\varphi=\pi$, there is no visible shift of the local energy minima away from this point. This observation is consistent with the absence of an anomalous Josephson current[31–33] for our specific field configuration (magnetic field parallel to the wire), in agreement with theoretical expectations[34–36].

In conclusion, we have presented microwave spectroscopy of Andreev bound states in semiconductor channels where the conductive modes are tuned by electrostatic gates, and we have demonstrated the effect of Zeeman splitting and spin–orbit coupling. The microwave spectroscopy measurements shown here could provide a new tool for quantitative studies of Majorana bound states, complementing quasiparticle tunnelling experiments[12,24]. Furthermore, we have provided direct evidence for the time-reversal symmetry breaking of the Andreev bound state spectrum in a multichannel ballistic system. This result paves the way to novel Josephson circuits, where the critical current depends on the current direction, leading to supercurrent rectification effects[37,38] tuned by electrostatic gates.

Data availability. The datasets generated and analysed during this study are available at the 4TU.ResearchData repository, DOI: http://dx.doi.org/10.4121/uuid:8c4a0604-ac00-4164-a37a-dad8b9d2f580 (ref. 39).

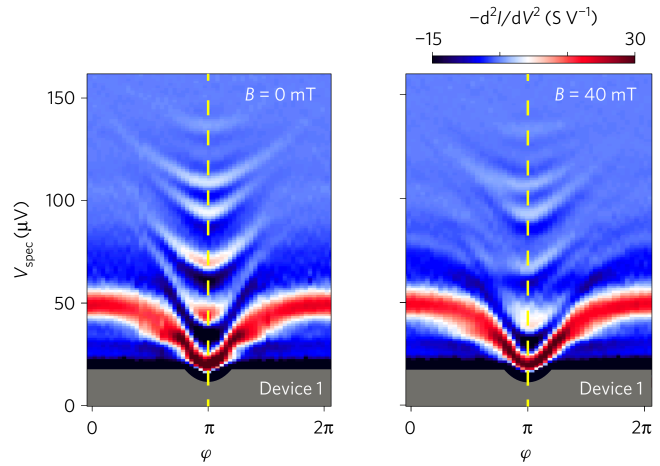

Figure 5 | Time-reversal symmetry-broken ABS in magnetic field. The symmetry axis at $\varphi=\pi$ at zero magnetic field is denoted by yellow dashed line. Note that at $B=40$ mT the observed spectrum does not obey the mirror symmetry with respect to the same line. The data was taken on device 1 at $V_g=-20$ mV. Grey regions denote lack of data due to bias instability of the circuit.

Received 1 September 2016; accepted 25 April 2017; published online 5 June 2017

References

1. Landauer, R. Can a length of perfect conductor have a resistance? *Phys. Lett. A* **85,** 91–93 (1981).
2. Kulik, I. O. Macroscopic quantization and the proximity effect in SNS junctions. *Sov. J. Exp. Theor. Phys.* **30,** 944–950 (1970).
3. Beenakker, C. W. J. Universal limit of critical-current fluctuations in mesoscopic Josephson junctions. *Phys. Rev. Lett.* **67,** 3836–3839 (1991).
4. Bretheau, L., Girit, Ç. Ö., Pothier, H., Esteve, D. & Urbina, C. Exciting Andreev pairs in a superconducting atomic contact. *Nature* **499,** 312–315 (2013).
5. Pillet, J.-D. *et al*. Andreev bound states in supercurrent-carrying carbon nanotubes revealed. *Nat. Phys.* **6,** 965–969 (2010).
6. Chang, W., Manucharyan, V., Jespersen, T. S., Nygård, J. & Marcus, C. M. Tunneling spectroscopy of quasiparticle bound states in a spinful Josephson junction. *Phys. Rev. Lett.* **110,** 217005 (2013).
7. Kos, F., Nigg, S. E. & Glazman, L. I. Frequency-dependent admittance of a short superconducting weak link. *Phys. Rev. B* **87,** 174521 (2013).
8. Janvier, C. *et al*. Coherent manipulation of Andreev states in superconducting atomic contacts. *Science* **349,** 1199–1202 (2015).
9. Väyrynen, J. I., Rastelli, G., Belzig, W. & Glazman, L. I. Microwave signatures of Majorana states in a topological Josephson junction. *Phys. Rev. B* **92,** 134508 (2015).
10. Lutchyn, R. M., Sau, J. D. & Das Sarma, S. Majorana fermions and a topological phase transition in semiconductor–superconductor heterostructures. *Phys. Rev. Lett.* **105,** 077001 (2010).
11. Oreg, Y., Refael, G. & von Oppen, F. Helical liquids and Majorana bound states in quantum wires. *Phys. Rev. Lett.* **105,** 177002 (2010).
12. Mourik, V. *et al*. Signatures of Majorana fermions in hybrid superconductor-semiconductor nanowire devices. *Science* **336,** 1003–1007 (2012).
13. Krogstrup, P. *et al*. Epitaxy of semiconductor-superconductor nanowires. *Nat. Mater.* **14,** 400–406 (2015).
14. Holst, T., Esteve, D., Urbina, C. & Devoret, M. H. Effect of a transmission line resonator on a small capacitance tunnel junction. *Phys. Rev. Lett.* **73,** 3455–3458 (1994).
15. Ambegaokar, V. & Baratoff, A. Tunneling between superconductors. *Phys. Rev. Lett.* **10,** 486–489 (1963).
16. Chang, W. *et al*. Hard gap in epitaxial semiconductor-superconductor nanowires. *Nat. Nanotech.* **10,** 232–236 (2015).
17. Doh, Y.-J. *et al*. Tunable supercurrent through semiconductor nanowires. *Science* **309,** 272–275 (2005).
18. Larsen, T. W. *et al*. Semiconductor-nanowire-based superconducting qubit. *Phys. Rev. Lett.* **115,** 127001 (2015).
19. de Lange, G. *et al*. Realization of microwave quantum circuits using hybrid superconducting-semiconducting nanowire Josephson elements. *Phys. Rev. Lett.* **115,** 127002 (2015).
20. Bretheau, L. *et al*. Theory of microwave spectroscopy of Andreev bound states with a Josephson junction. *Phys. Rev. B* **90,** 134506 (2014).
21. Zazunov, A., Shumeiko, V. S., Bratus, E. N., Lantz, J. & Wendin, G. Andreev level qubit. *Phys. Rev. Lett.* **90,** 087003 (2003).
22. Zazunov, A., Shumeiko, V. S., Wendin, G. & Bratus, E. N. Dynamics and phonon-induced decoherence of Andreev level qubit. *Phys. Rev. B* **71,** 214505 (2005).
23. Cheng, M. & Lutchyn, R. M. Josephson current through a superconductor/semiconductor-nanowire/superconductor junction: effects of strong spin–orbit coupling and Zeeman splitting. *Phys. Rev. B* **86,** 134522 (2012).
24. Das, A. *et al*. Zero-bias peaks and splitting in an Al-InAs nanowire topological superconductor as a signature of Majorana fermions. *Nat. Phys.* **8,** 887–895 (2012).
25. Higginbotham, A. P. *et al*. Parity lifetime of bound states in a proximitized semiconductor nanowire. *Nat. Phys.* **11,** 1017–1021 (2015).
26. Albrecht, S. M. *et al*. Exponential protection of zero modes in Majorana islands. *Nature* **531,** 206–209 (2016).
27. Michelsen, J., Shumeiko, V. S. & Wendin, G. Manipulation with Andreev states in spin active mesoscopic Josephson junctions. *Phys. Rev. B* **77,** 184506 (2008).
28. Nijholt, B. & Akhmerov, A. R. Orbital effect of magnetic field on the Majorana phase diagram. *Phys. Rev. B* **93,** 235434 (2016).
29. Meservey, R. & Tedrow, P. Properties of very thin aluminum films. *J. Appl. Phys.* **42,** 51–53 (1971).
30. Yokoyama, T., Eto, M. & Nazarov, Y. V. Josephson current through semiconductor nanowire with spin–orbit interaction in magnetic field. *J. Phys. Soc. Jpn* **82,** 054703 (2013).
31. Krive, I. V., Gorelik, L. Y., Shekhter, R. I. & Jonson, M. Chiral symmetry breaking and the Josephson current in a ballistic superconductor–quantum wire–superconductor junction. *Low Temp. Phys.* **30,** 398–404 (2004).
32. Buzdin, A. Direct coupling between magnetism and superconducting current in the Josephson φ_0 junction. *Phys. Rev. Lett.* **101,** 107005 (2008).
33. Szombati, D. B. *et al*. Josephson φ_0-junction in nanowire quantum dots. *Nat. Phys.* **12,** 568–572 (2016).
34. Liu, J.-F. & Chan, K. S. Relation between symmetry breaking and the anomalous Josephson effect. *Phys. Rev. B* **82,** 125305 (2010).
35. Rasmussen, A. *et al*. Effects of spin–orbit coupling and spatial symmetries on the Josephson current in SNS junctions. *Phys. Rev. B* **93,** 155406 (2016).
36. Konschelle, F., Tokatly, I. V. & Bergeret, F. S. Theory of the spin-galvanic effect and the anomalous phase shift φ_0 in superconductors and Josephson junctions with intrinsic spin–orbit coupling. *Phys. Rev. B* **92,** 125443 (2015).
37. Villegas, J. E. *et al*. A superconducting reversible rectifier that controls the motion of magnetic flux quanta. *Science* **302,** 1188–1191 (2003).
38. Reynoso, A. A., Usaj, G., Balseiro, C. A., Feinberg, D. & Avignon, M. Anomalous Josephson current in junctions with spin polarizing quantum point contacts. *Phys. Rev. Lett.* **101,** 107001 (2008).
39. van Woerkom, D. J. *et al*. *Microwave Spectroscopy of Spinful Andreev Bound States in Ballistic Semiconductor Josephson Junctions* (QuTech, 2017); http://doi.org/b6xg

Acknowledgements

The authors thank L. Bretheau, Ç. Ö. Girit, L. DiCarlo, M. P. Nowak and A. R. Akhmerov for fruitful discussions, and R. van Gulik, T. Kriváchy, A. Bruno, N. de Jong, J. D. Watson, M. C. Cassidy, R. N. Schouten and T. S. Jespersen for assistance with fabrication and experiments. This work has been supported by the Danish National Research Foundation, the Villum Foundation, the Dutch Organization for Fundamental Research on Matter (FOM), the Netherlands Organization for Scientific Research (NWO) by a Veni grant, Microsoft Corporation Station Q and a Synergy Grant of the European Research Council. B.v.H. was supported by ONR Grant Q00704. L.I.G. and J.I.V. acknowledge the support by NSF Grant DMR-1603243.

Author contributions

D.J.v.W., A.P. and D.B. performed the experiments. B.v.H., J.I.V. and L.I.G. developed the theory to analyse the data. P.K. and J.N. contributed to the nanowire growth. D.J.v.W., A.P. and D.B. fabricated the samples. L.P.K. and A.G. designed and supervised the experiments. D.J.v.W., B.v.H., L.P.K. and A.G. analysed the data. The manuscript has been prepared with contributions from all the authors.

Additional information

Supplementary information is available in the online version of the paper. Reprints and permissions information is available online at www.nature.com/reprints. Publisher's note: Springer Nature remains neutral with regard to jurisdictional claims in published maps and institutional affiliations. Correspondence and requests for materials should be addressed to A.G.

Competing financial interests

The authors declare no competing financial interests.